



HAL
open science

Influence of galactic arm scale dynamics on the molecular composition of the cold and dense ISM III. Elemental depletion and shortcomings of the current physico-chemical models

V. Wakelam, W. Iqbal, J.-P. Melisse, P. Gratier, M. Ruaud, I. Bonnell

► **To cite this version:**

V. Wakelam, W. Iqbal, J.-P. Melisse, P. Gratier, M. Ruaud, et al.. Influence of galactic arm scale dynamics on the molecular composition of the cold and dense ISM III. Elemental depletion and shortcomings of the current physico-chemical models. Monthly Notices of the Royal Astronomical Society, 2020, 497 (2), pp.2309-2319. 10.1093/mnras/staa2016 . hal-02973012

HAL Id: hal-02973012

<https://hal.science/hal-02973012>

Submitted on 21 May 2024

HAL is a multi-disciplinary open access archive for the deposit and dissemination of scientific research documents, whether they are published or not. The documents may come from teaching and research institutions in France or abroad, or from public or private research centers.

L'archive ouverte pluridisciplinaire **HAL**, est destinée au dépôt et à la diffusion de documents scientifiques de niveau recherche, publiés ou non, émanant des établissements d'enseignement et de recherche français ou étrangers, des laboratoires publics ou privés.

Influence of galactic arm scale dynamics on the molecular composition of the cold and dense ISM III. Elemental depletion and shortcomings of the current physico-chemical models

V. Wakelam ¹★, W. Iqbal,² J.-P. Melisse,¹ P. Gratier ¹, M. Ruaud³ and I. Bonnell⁴

¹Laboratoire d'astrophysique de Bordeaux, Univ. Bordeaux, CNRS, B18N, allée Geoffroy Saint-Hilaire, F-33615 Pessac, France

²South-Western Institute for Astronomy Research (SWIFAR), Yunnan University (YNU), Kunming 650500, People's Republic of China

³NASA Ames Research Center, Moffett Field, CA 94035, USA

⁴Scottish Universities Physics Alliance (SUPA), School of Physics and Astronomy, University of St. Andrews, North Haugh, St Andrews, Fife KY16 9SS, UK

Accepted 2020 July 7. Received 2020 July 7; in original form 2020 January 14

ABSTRACT

We present a study of the elemental depletion in the interstellar medium. We combined the results of a Galactic model describing the gas physical conditions during the formation of dense cores with a full-gas-grain chemical model. During the transition between diffuse and dense medium, the reservoirs of elements, initially atomic in the gas, are gradually depleted on dust grains (with a phase of neutralization for those which are ions). This process becomes efficient when the density is larger than 100 cm^{-3} . If the dense material goes back into diffuse conditions, these elements are brought back in the gas phase because of photo-dissociations of the molecules on the ices, followed by thermal desorption from the grains. Nothing remains on the grains for densities below 10 cm^{-3} or in the gas phase in a molecular form. One exception is chlorine, which is efficiently converted at low density. Our current gas–grain chemical model is not able to reproduce the depletion of atoms observed in the diffuse medium except for Cl, which gas abundance follows the observed one in medium with densities smaller than 10 cm^{-3} . This is an indication that crucial processes (involving maybe chemisorption and/or ice irradiation profoundly modifying the nature of the ices) are missing.

Key words: astrochemistry – ISM: abundances – ISM: atoms – ISM: evolution.

1 INTRODUCTION

After the big bang, the very first stars formed only from hydrogen (H) and helium (He). Heavier elements are formed later, either through fusion inside stars or by neutron capture processes in supernovae explosion or neutron star mergers. At the end of the life of a star, some of the ejected atoms form refractory dust, others remain in the gas phase. This material is included in the cycle of interstellar matter: forming denser regions up to molecular clouds, newly stars, and planetary systems, until the star dies and spreads its inner material into the diffuse interstellar medium (ISM) again. Within this cycle, chemical elements can be found in three phases: (a) in the gas phase, (b) in the refractory grain cores, and (c) in the icy mantles of grains. The sum of abundance of the elements contained in all three phases is called the cosmic elemental abundance. Cosmic abundances are assumed to represent some reference value and are measured in the atmosphere of stars (our Sun or other stars) (see, for instance, Sofia, Cardelli & Savage 1994; Asplund et al. 2009).

In the diffuse medium, no icy mantles are expected to be present on grains and so the measured abundances of gas-phase elements (which are mostly in the ionized form except for O, N, and F) subtracted from these cosmic abundances should give the amount of each element stored in the refractory cores and so not available for any volatile

chemistry. Observations of gas-phase atomic lines towards different lines of sight indicate that the depletion of the elements from the gas phase increases with the density of the cloud, even when the density of the cloud remains too low to explain the depletion simply by collisions with grains (Savage & Sembach 1996; Jenkins 2009). Silicon, for instance, has a cosmic elemental abundance of 3.5×10^{-5} (compared to H; Asplund et al. 2009). The gas-phase abundance Si^+ measured in clouds with densities of about 10^{-2} cm^{-3} is 2×10^{-5} and drops by a factor of 10 at densities of 10 cm^{-3} . This observed decrease of the atomic abundance in the gas phase could be related to a more efficient neutralization of the cations (since what is measured is Si^+), but at such low densities, only dielectronic recombination or ion–molecule reactions could really alter the balance of ion stages as it is the case for a small number of elements (Savage & Sembach 1996). Observations of atomic lines in diffuse clouds can be done only for densities below 10 cm^{-3} because at higher density, the atomic lines become optically thick. In dense molecular clouds (with densities of a few 10^4 cm^{-3}), SiO was not detected (upper limit of $\sim 2 \times 10^{-12}$ compared to H; Ziurys, Friberg & Irvine 1989), indicating that the depletion of silicon continues at densities larger than 10 cm^{-3} .

The mechanism of depletion can simply be understood as a matter of collision between gas-phase species and grains. At a density of 10 cm^{-3} for a gas temperature of 100 K, the typical adsorption time is about 10^8 yr , which is of the same order as the typical lifetime of interstellar grains in the ISM (Draine 2009).

* E-mail: valentine.wakelam@u-bordeaux.fr

At lower density, the adsorption time-scale may be longer and turbulent mixing may play a role in driving dust from denser regions (Tielens 1998). The chemistry associated with this depletion and the resulting species are still a matter of debate (see, for instance, Tielens 1998; Whittet 2010). Whittet (2010), for instance, debated on the depletion of oxygen at different densities. Summing all the observed volatile phases of oxygen and the oxygen presumably contained in the refractory parts of the grains, Whittet found that approximately 28 per cent of the oxygen could not be accounted for, calling this fraction the unidentified depleted oxygen. This very specific problem of the elemental depletion in tenuous regions (with densities below a few 10^3 cm^{-3}) is particularly important for the chemistry of dense regions such as star and planetary system-forming regions. In fact, the fraction of the elements available for phases (a – gas phase) and (c – ice mantle), i.e. only phases that can be observed in star-forming regions, is determined by what is depleted in phase (b – grain core), which is quite uncertain. Considering the uncertainties in the fraction of elements still available, various values are used in astrochemical models and sometime adjusted to reproduce observations.

In this paper, we explore this problem coupling time-dependent simulations of the gas physical conditions following the transition between diffuse and dense interstellar regions with a detailed gas–grain chemical model. In two previous papers, we have already analysed these simulations to show (1) the chemical diversity of cold cores induced by the variety of physical histories experienced by the gas and the dust forming such structures (Ruaud et al. 2018), and (2) the impact of these histories in the interstellar O_2 abundance (Wakelam et al. 2019).

2 MODELS DESCRIPTION

To simulate the chemistry during the formation of cold cores, we used the physical structure provided by the 3D smoothed-particle hydrodynamics (SPH) galactic model from Bonnell, Dobbs & Smith (2013). In these simulations, the gas from the spiral arm is cold ($T_{\text{gas}} < 100 \text{ K}$) and $n_{\text{H}} \sim 100 \text{ cm}^{-3}$, while gas entering comprises warm gas ($T_{\text{gas}} < 8000 \text{ K}$) and some cooler and denser gas from previous spiral arm encounters (Bonnell et al. 2013; Ruaud et al. 2018). Dense clouds are formed by converging flows when the interstellar gas enters the spiral arms. The gas is shocked and compressed, which heats the gas, balanced against the increased atomic cooling rates at the higher densities (Bonnell et al. 2013, and see also Vázquez-Semadeni et al. 2007; Koyama & Inutsuka 2002). Ultimately, the cooling dominates and results in cold dense gas susceptible to gravitational collapse (see also Larson 2005). Bonnell et al. (2013) presented three types of simulations with three different spatial resolutions from the scale of a spiral galaxy, to the formation of dense clouds in the ISM, to the relatively small, sub-pc scale where star formation occurs. To keep the computational time reasonable, only the highest resolution sub-pc scale simulations include self-gravity. For the purpose of this work (because we are not interested in the collapse phase and we want to study the effect of the dense gas being brought back into the diffuse medium), we have used the ‘medium’ spatial resolution, which does not include self-gravity such that if the external pressure decreases, the cool gas can re-expand and warm up. The SPH model gives us the gas temperature and density as a function of time and position in space. Using this information, we computed visual extinctions and dust temperatures as explained in Ruaud et al. (2018). At the end of the simulations, 12 clouds were identified with a maximum peak density above 10^5 cm^{-3} . We then identified all the SPH particles

Table 1. Elemental abundances (with respect to the total hydrogen density) used in the simulations. The values are from Jenkins (2009) for a depletion factor (F^*) of zero except for Na and F for which we used the solar abundances from Asplund et al. (2009).

Atoms	Abundance
He	9×10^{-2}
N	6.2×10^{-5}
O	5.6×10^{-4}
C	2.4×10^{-4}
S	1.3×10^{-5}
Si	2.4×10^{-5}
Fe	3.9×10^{-6}
Na	1.7×10^{-6}
Mg	2.2×10^{-5}
P	6.8×10^{-7}
Cl	5.9×10^{-7}
F	3.6×10^{-8}

in a sphere of 0.5 pc around this maximum and retrieved the past and future history of these particles. The physical conditions of each of the particles were used as input parameters at each time-step of the Nautilus three-phase gas–grain model (Ruaud, Wakelam & Hersant 2016). In total, we have approximately 3000 trajectories describing the physical and chemical evolution of parcels of material in a galactic arm going from very diffuse conditions (below 0.1 cm^{-3}) to dense ones (of a few 10^5 cm^{-3}). The SPH model does not include self-gravity, so the clouds are always dissipated after reaching the maximum peak density. This allows us to study the effect of cycles between dense and less dense ISM, which were suggested by Draine (2009) as an explanation for elemental depletion. While exposing the results, we will make a distinction between the first phase of the simulation (the increase of the density with time up to a maximum value) and a second phase that begins when the cloud starts to dissipate and the density decreases again. More details on the methodology can be found in Ruaud et al. (2018). Details on the chemical model and the chemical parameters are in Wakelam et al. (2019). Analysis of the results of the physical model is done in Bonnell et al. (2013) and in a paper currently in preparation. The cosmic ray ionization rate is kept constant to 10^{-17} s^{-1} for simplicity. Determining the charge of the interstellar grains is complex and it depends on many parameters relative to the grains themselves (size, nature, etc.) and on the physical properties of the environment (UV field, density, temperature) (Bel et al. 1989). To limit the computational time, the astrochemical model used in these simulations assumes only one single grain size and the grains can be either neutral or negatively charged. Only neutral gas-phase species are allowed to stick on the grains as the grains are supposed to be mostly negatively charged when the density is above 10^3 cm^{-3} (Bel et al. 1989). We do not take into account the possible sticking of ions on neutral grains. This means that we may overestimate the time-scale of depletion of atoms on the grains as it may occur earlier in the simulations. At the lowest densities, however, the electronic recombination of ionized atoms should be faster than the collision with grains.

Table 1 lists the elemental abundances used in the model. These values correspond to abundances observed in the most diffuse regions in Jenkins (2009) sample where they observed the smallest depletion (their $F^* = 0$). These values are smaller than the solar abundances as the fraction of elements included in the refractory grains produced by stars has already disappeared. Two elements are not included in

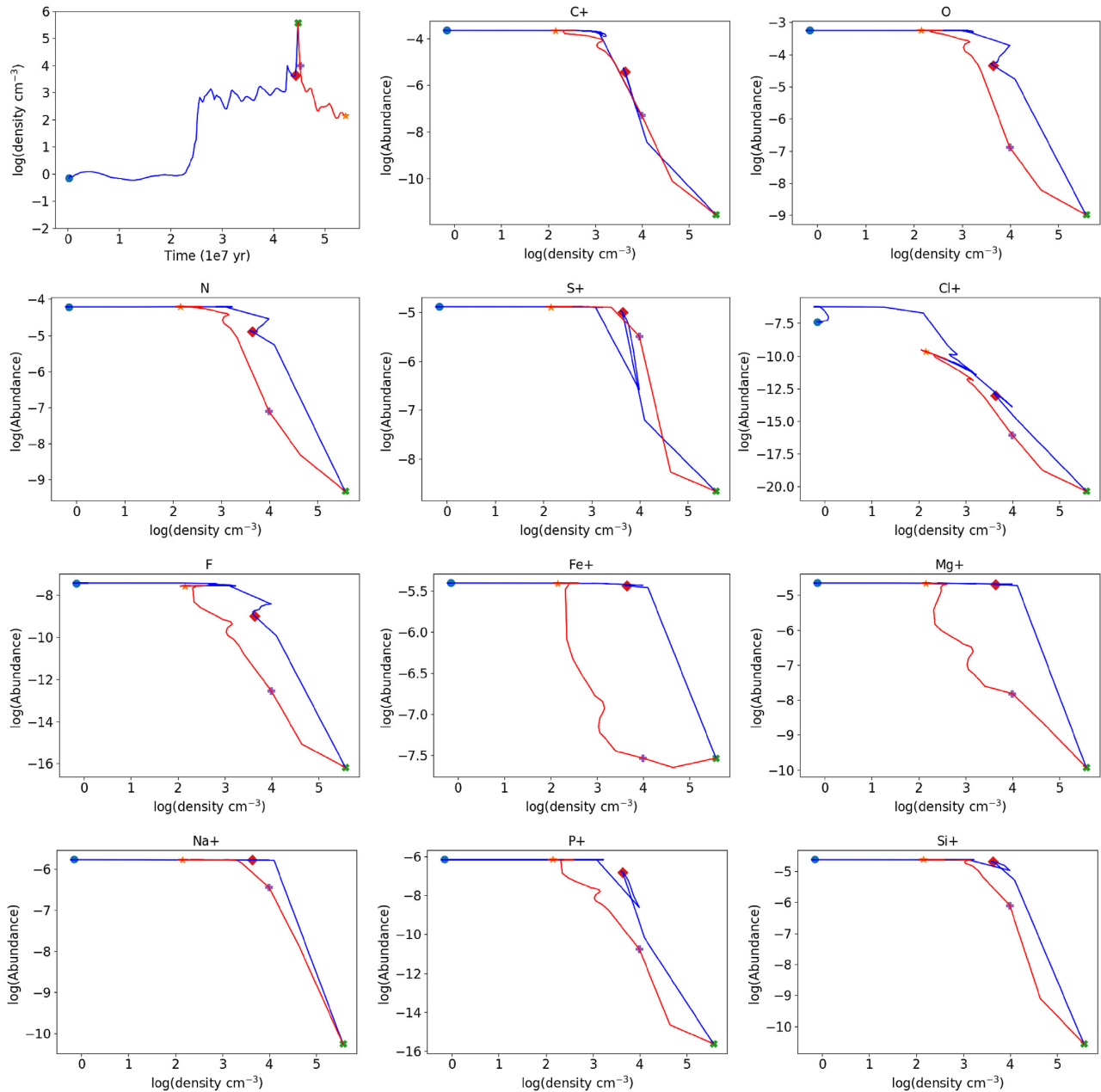


Figure 1. Density as a function of time for trajectory A (upper left-hand panel) and gas-phase atomic abundances (X) as a function of density for the same trajectory for the rest of the figure. Symbols are just markers to help reading the time dependency of the figures. Blue and red parts of the lines represent the phase of increasing and decreasing density.

Jenkins (2009) study: Na and F. For these two ones, we have used the solar abundance from Asplund et al. (2009).

3 RESULTS

In our simulations, we obtain the chemical evolution for thousands of parcel of material, each experiencing different physical conditions, that changes with time. It is not possible to describe the behaviour of the species and the chemical processes at play for each of them as we have a large spread of the chemical compositions as was shown in previous publications (Ruaud et al. 2018; Wakelam et al. 2019). We will then first

show the examples for two selected trajectories and give more general statistical results considering all of them in a second subsection.

3.1 Two individual trajectories

To visualize the results, we first show in Figs 1 and 2 the density as a function of time for two selected trajectories and the associated atomic gas-phase abundances as a function of density. These two trajectories are the same as in Wakelam et al. (2019). The dust and gas temperatures as a function of time for the two trajectories are shown in Appendix A (Figs A1 and A2). On the figures, we use

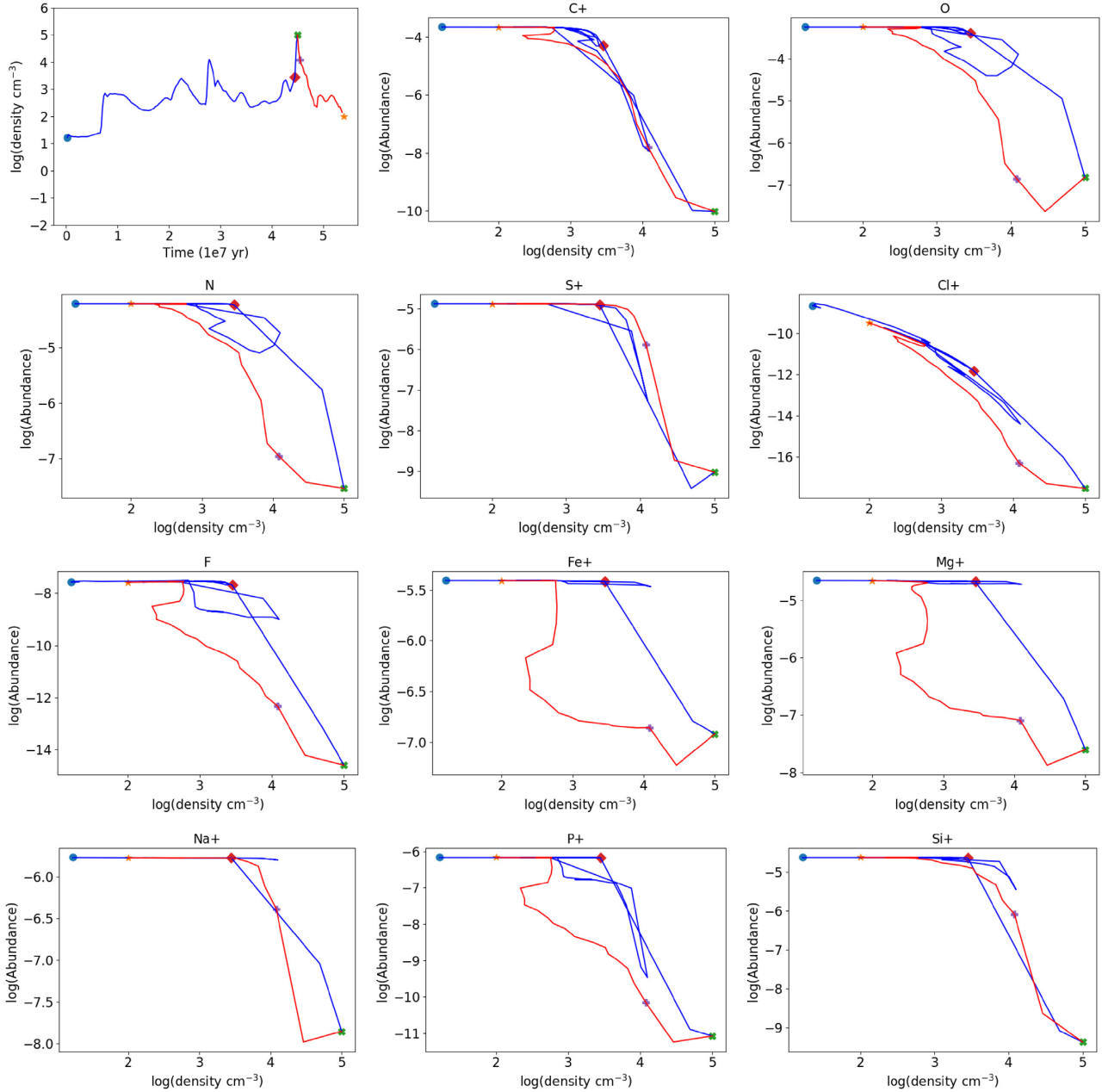


Figure 2. Density as a function of time for trajectory B (upper left-hand panel) and gas-phase atomic abundances (X) as a function of density for the same trajectory for the rest of the figure. Symbols are just markers to help reading the time dependency of the figures. Blue and red parts of the lines represent the phase of increasing and decreasing density.

markers to help identifying the initial and final times, as well as the peak density (at 4.45×10^7 yr for both). The time-step of physical changes is given by the SPH model (2.35×10^5 yr). The maximum pic density is then not much resolved representing only a few points. To test the effect of this, we have doubled the number of temporal points by interpolating between two SPH points and run again the model for a few trajectories. The results are not changed significantly. In these two examples presented here, as in all the other trajectories, the evolution of the density is not linear, resulting in chaotic profiles when looking at the abundance of the atoms as a function of density. The two trajectories do not have the same history of density resulting in a difference in the atomic abundances as a function of density. The starting density of A (0.7 cm^{-3}) is smaller than for B (9 cm^{-3}), the

maximum density is $3.7 \times 10^5 \text{ cm}^{-3}$ for A while it is $9.3 \times 10^4 \text{ cm}^{-3}$ for B, and the final density is 125 cm^{-3} for A and 56 cm^{-3} for B. For both trajectories, except for Cl^+ , the atomic abundances are rather flat until the density reaches a few 10^3 or a few 10^4 cm^{-3} depending on the species. Then the abundances decrease before increasing again when the density decreases. All elements show a minimum at the density peak or just after. In the cases where the minimum abundances do not coincide with the maximum density, the depletion time-scale is longer than the evolution of the density. The time-scale for the species to come back into the gas phase depends on the physical conditions, i.e. different for each trajectory. The chaotic behaviour of the results makes it difficult to describe generic results concerning the chemistry.

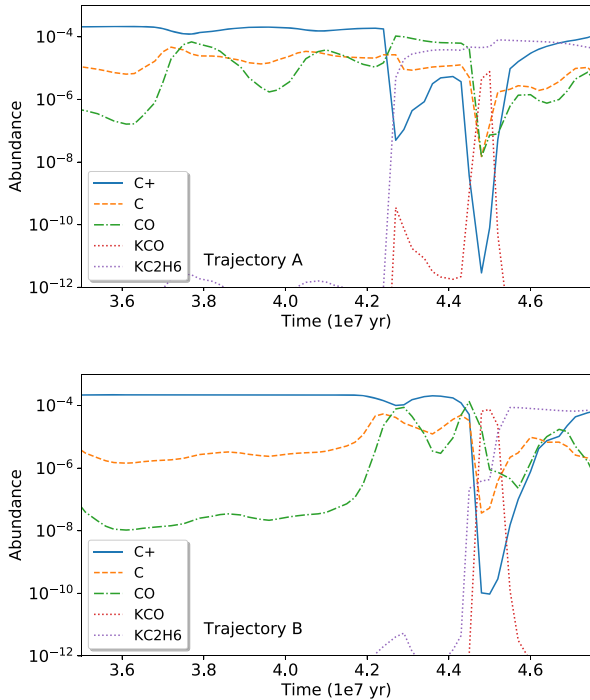


Figure 3. Abundance of the main carbon carriers as a function of time for trajectories A (upper panel) and B (lower panel). K means species in the ices.

For elements with complex chemistry, such as carbon, oxygen, nitrogen, and sulphur, the elements can be spread over many different species and these species will not be the same for all conditions because it depends on the history (Ruaud et al. 2018). We show in Fig. 3 the abundance of the main carriers of carbon as a function of time for both trajectories. In trajectory A, between 2.5×10^7 and 4.2×10^7 yr, C^+ dominates, but C and CO are also abundant. During this time, in trajectory B, C and CO are much less abundant than in A, probably because the density is smaller. In A, however, the increase of the density at 4.2×10^7 yr is faster than in B so that the C^+ abundance drops faster while it remains high for a longer period of time in B. At the same time (when C^+ drops), gas-phase CO becomes the major carrier of carbon for approximately 2×10^6 yr in trajectory A. Then at about 4.5×10^7 yr, most of the carbon is locked into C_2H_6 ice. In trajectory B, at $\sim 4.4 \times 10^7$ yr, most of the carbon is first in CO ice for a small amount of time and then in C_2H_6 ice. In both models, C^+ becomes a reservoir again when the density decreases. Oxygen is less complicated as atomic oxygen and water carry the majority of the element. The drop of gas-phase atomic oxygen happens later (after 4.4×10^7 yr) in B while it happens at 4.2×10^7 yr in A. The nitrogen gas-phase atomic abundance drops approximately at the same time as for O. Later, NH_3 and HCN ices carry most of the nitrogen but not with the same amount and not at the same time for the two trajectories (see Fig. 4). For sulphur (Fig. 5), we also see a decrease of gas-phase S^+ at the same time as O and N but S^+ and S alternatively share most of the sulphur between 4.2×10^7 and 4.4×10^7 yr before forming HS and H_2S ices for trajectory A. This alternance of S^+ and S is not seen for trajectory B.

For Fe, Mg, Na, and Si, which are initially ionic, the decrease in abundance is first due to the electronic recombination with electrons (this is in fact also the case for C and S). The neutral atoms are then depleted on interstellar grains during collision and hydrogenated. As such, FeH, MgH_2 , NaH, and SiH_4 ices are the main carriers of

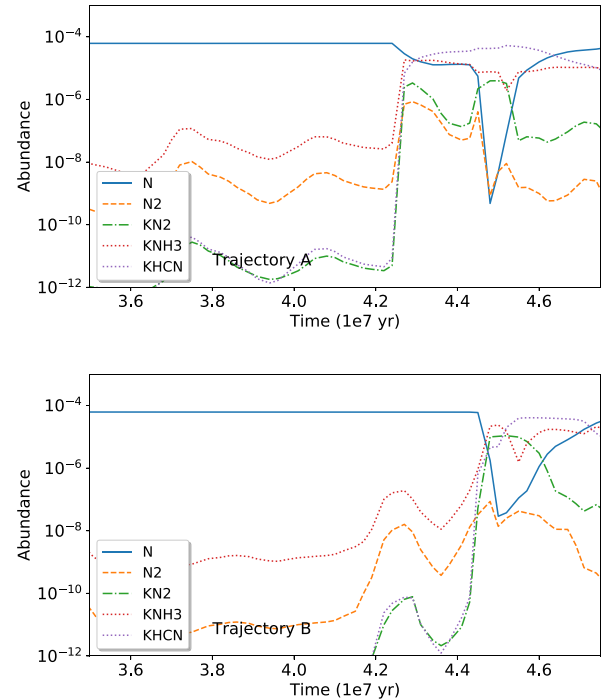


Figure 4. Abundance of the main nitrogen carriers as a function of time for trajectories A (upper panel) and B (lower panel). K means species in the ices.

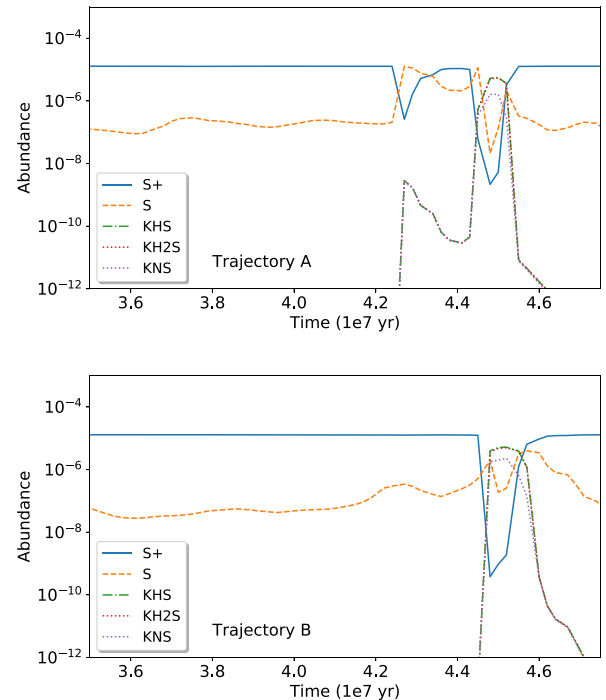


Figure 5. Abundance of the main sulphur carriers as a function of time for trajectories A (upper panel) and B (lower panel). K means species in the ices.

these elements at high density. The case of iron is shown in Fig. 6. F and P^+ react mostly with H_2 to form HF and PH_2^+ . HF then depletes on the grains while PH_2^+ reacts with electrons to produce P (and PH but PH gives P through the reactions $PH + C^+ \rightarrow PH^+ + C$ and $PH^+ + e^- \rightarrow P + H$). Atomic neutral phosphorus then

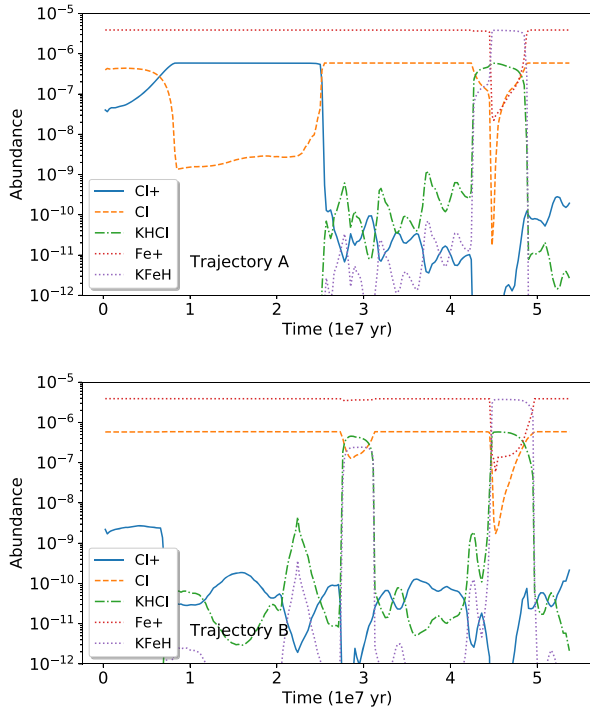


Figure 6. Abundances of the main chlorine and iron carriers as a function of time for trajectories A (upper panel) and B (lower panel). K means species in the ices. Note that the x -axis is not the same as for Figs 3–5.

depletes on the grains and is hydrogenated into PH_3 . HF and PH_3 ices are the main carriers of fluorine and phosphorus at high density. Chlorine appears as an exception here because the Cl^+ gas-phase abundance drops at much smaller density (see Fig. 6) as compared to the other elements. This fast $\text{Cl}^+ \rightarrow \text{Cl}$ conversion is due to the combined effect of the electronic recombination of Cl^+ ($\text{Cl}^+ + e^- \rightarrow \text{Cl} + h\nu$) and the $\text{Cl}^+ + \text{H}_2 \rightarrow \text{HCl}^+ + \text{H}$ reaction (followed by $\text{HCl}^+ + \text{H}_2 \rightarrow \text{H}_2\text{Cl}^+ + \text{H}$ and $\text{H}_2\text{Cl}^+ + e^- \rightarrow \text{Cl} + 2\text{H}$). We checked this hypothesis by decreasing each and then both rate coefficients. The rate coefficient of the electronic recombination of Cl^+ , in our network, is $1.13 \times 10^{-10} (T/300)^{-0.7} \text{ cm}^3 \text{ s}^{-1}$. This rate coefficient is more than one order of magnitude larger than the typical electronic recombination included in astrochemical data bases. This rate coefficient is indicated in the KIDA data base¹ (Wakelam et al. 2012) and comes from the 1991 version of UMIST² (Millar et al. 1991). In the last UMIST version (2012) (McElroy et al. 2013), it has been modified towards smaller values but without any reference. More laboratory work is required on this reaction. Decreasing the rate coefficient, however, does not significantly change the Cl^+ abundance as long as the $\text{Cl}^+ + \text{H}_2 \rightarrow \text{HCl}^+ + \text{H}$ rate coefficient stays high ($10^{-9} \text{ cm}^3 \text{ s}^{-1}$, Neufeld & Wolfire 2009). The two trajectories show different results for Cl. As the density is initially smaller in A, the gas-phase abundance of Cl^+ is high for about $2.5 \times 10^7 \text{ yr}$ while it is always low in B. Around $3 \times 10^7 \text{ yr}$, trajectory B experiences a bump in density high enough to produce large amounts of HCl ice but that is then dissociated and brought back into the gas phase as neutral Cl before the maximum density peak is achieved. At high density, HCl ices are the main carrier of chlorine.

¹<http://kida.obs.u-bordeaux1.fr/>

²<http://udfa.ajmarkwick.net/>

During the second phase, after the density peak, for the heavy elements with a simple chemistry (Mg, F, Fe, P, Si, Na, and Cl), the reservoirs stored on the grains are first dissociated on the surfaces as the density decreases. The atoms are then evaporated and ionized (except for fluorine). Photodesorption plays here a minor role. If the efficiency of the process scales with the visual extinction, the yield is small (10^{-4}) and the same for all species (Ruaud et al. 2016). Note that the fluorine atomic gas-phase abundance F in the two examples shown in Figs 1 and 2 represents only 67 percent of the elemental abundance at the end of the simulation. The remaining fluorine is in the form of HF in the gas because of a rapid $\text{F} + \text{H}_2 \rightarrow \text{H} + \text{HF}$ reaction. For smaller densities (as shown in the next section), HF eventually dissociates and F becomes the main fluorine carrier again.

3.2 All trajectories

As time is a model-dependent parameter, we plot the results as a function of density in Figs 7–9 for all trajectories. The abundances during the first phase (increasing density) are shown in the left and on the right for the second phase (decreasing density). Considering all trajectories, we find similar behaviour as previously shown. For most elements, the decrease in the atomic abundances starts when the density is larger than $\sim 10 \text{ cm}^{-3}$. Chlorine is an exception as its abundance decreases for some trajectories for densities below 0.1 cm^{-3} . Some of the trajectories do not show any elemental depletion at high density, except for Cl^+ , which is always depleted. This is because, within the full range of histories studied here, there are always trajectories presenting fast increase of the density, which induces a delay in the molecular depletion. Chlorine again does not present this behaviour because of its fast conversion to its neutral form in the gas phase. For all elements, the abundances in phase 2 (decreasing phase of density) are smaller at low density than in phase 1 (increasing phase of density), meaning that the depletion experienced in the dense phase impacts the inventory of available gas-phase elements in phase 2. This effect is stronger for C^+ , Fe^+ , Mg^+ , P^+ , Cl^+ , and F. Later on, the gas abundances of Mg^+ , P^+ , F, Si^+ , Fe^+ , and Na^+ are equal to the initial abundances used in the model when the density is smaller than 10 cm^{-3} .

On Figs 7–9, we have superimposed the elemental depletion laws derived by Jenkins (2009) from atomic-line observations in the diffuse ISM (up to 10 cm^{-3}). For carbon, oxygen, and nitrogen, the observed elemental abundance is small and not in contradiction with our predictions. For iron, magnesium, phosphorus, and silicon, the observed depletion is much stronger than predicted by the model. For chlorine, we do reproduce the observed depletion.

4 DISCUSSION AND CONCLUSION

In this paper, we studied the depletion of the elements during the transition between the diffuse and dense ISM by coupling a full gas–grain chemical model to results obtained from large-scale hydrodynamics simulations of the ISM at galactic scales. With this approach, we could follow the evolution of interstellar matter over several millions of years and study the effect of cycling between low-density and high-density phases on the depletion of elements such as C, O, N, S, Si, Fe, Na, Mg, P, Cl, and F. For all these elements, we find that the strength of their depletion is set by the balance between accretion/reactions at the surface and their ability to resist photoprocessing. Our main result is that all these elements, but Cl, recover their undepleted values when $n_{\text{H}} < 10 \text{ cm}^{-3}$, and our model

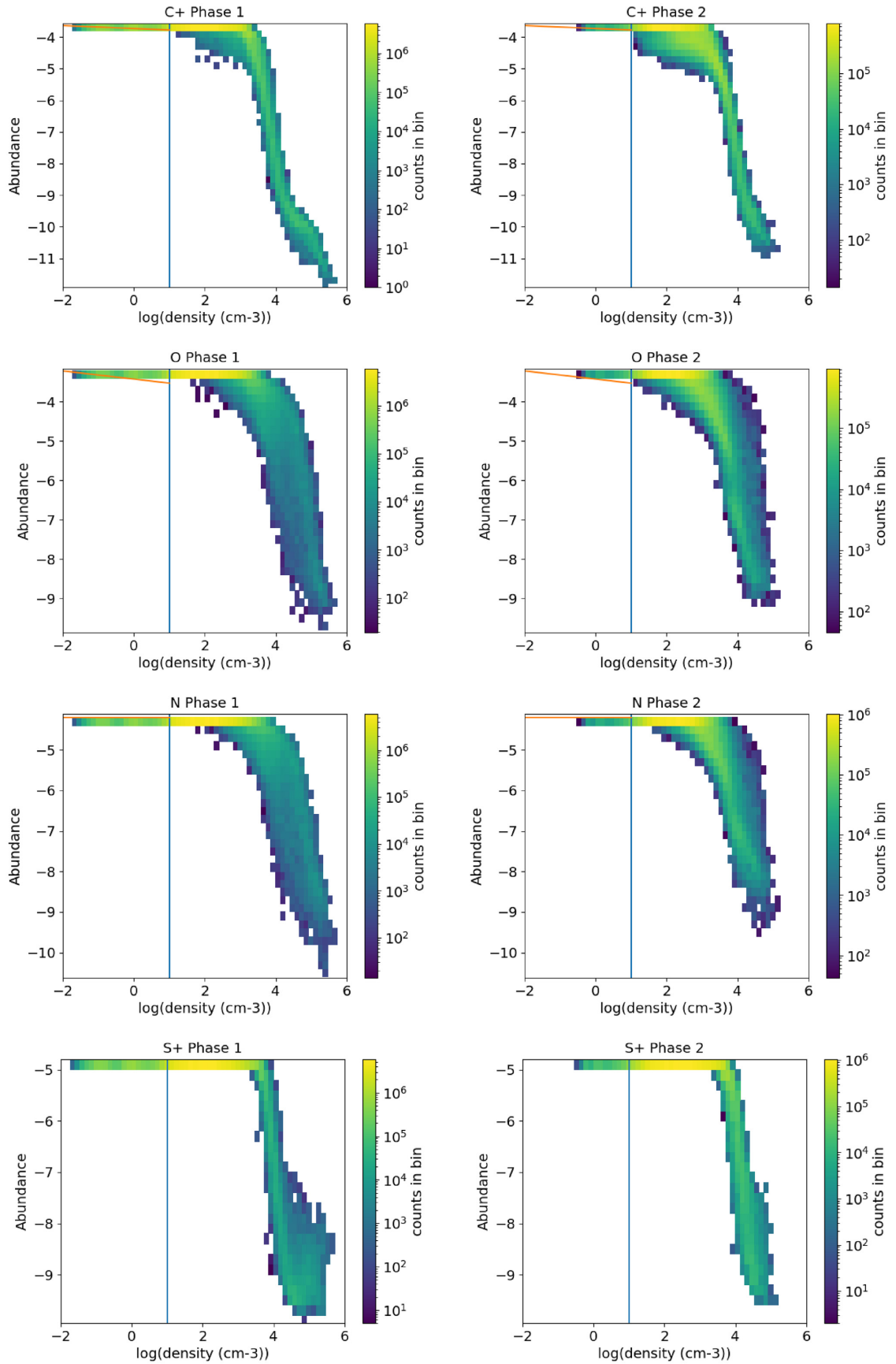


Figure 7. Abundances as a function of density for phase 1 [left – (increasing phase of density)] and phase 2 [right – (decreasing phase of density)]. The vertical line locates the 10 cm⁻³ density. The red lines show the depletion laws from Jenkins (2009).

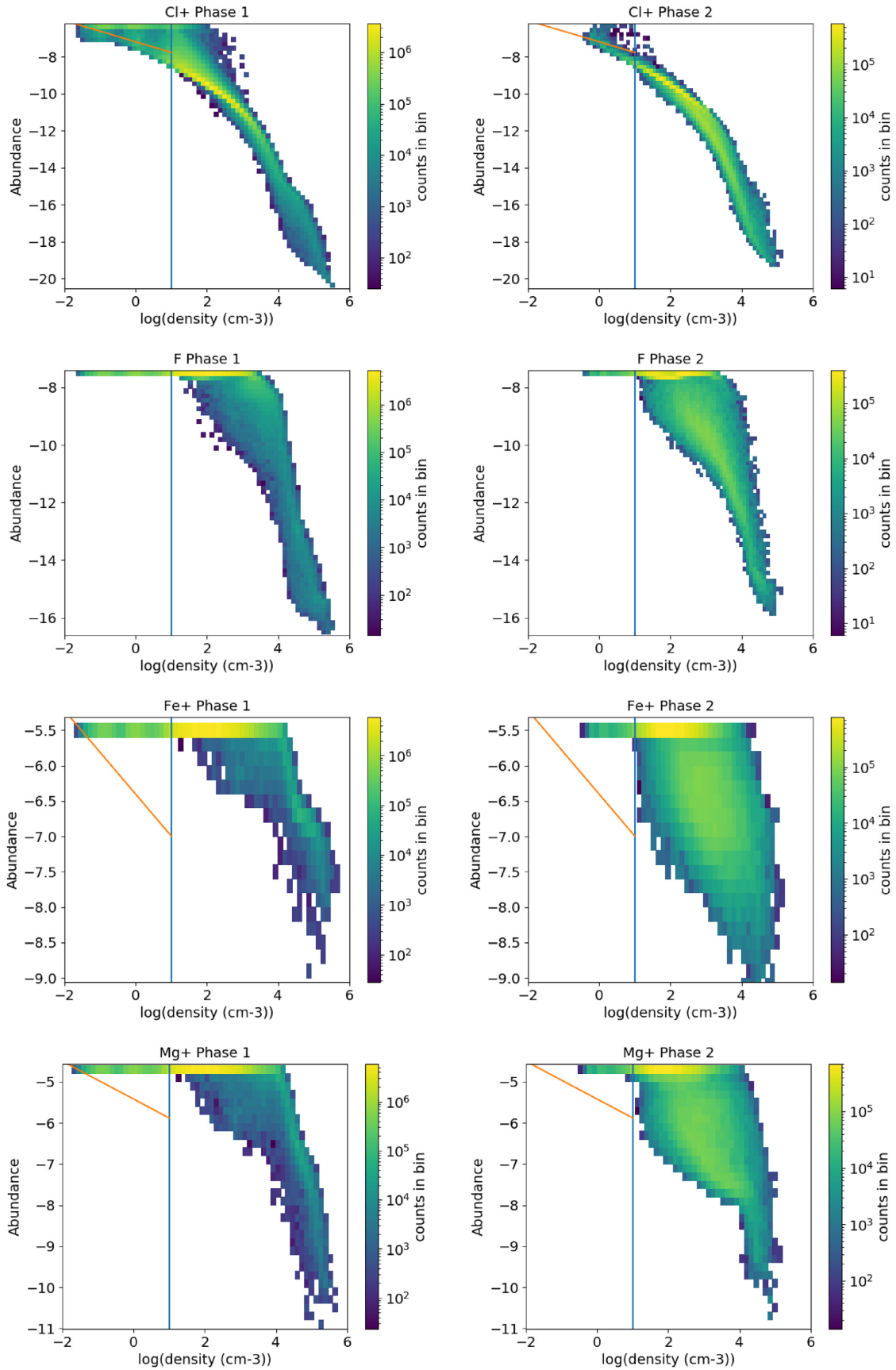


Figure 8. Same as Fig. 7.

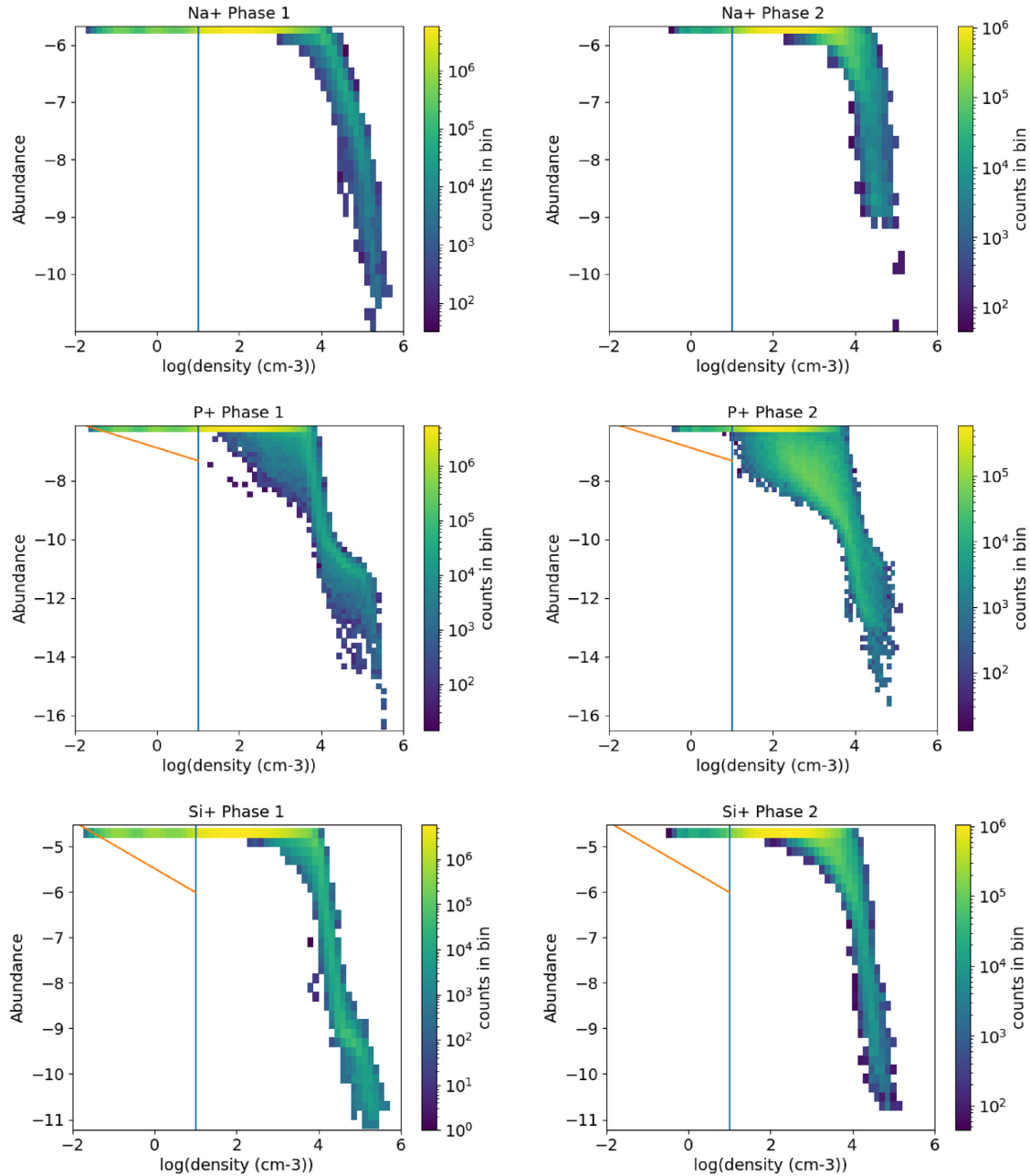


Figure 9. Same as Fig. 7.

thus fails at reproducing depletion patterns derived from observations of low-density gas (Jenkins 2009).

Chlorine is an exception and the depletion pattern of Cl^+ at $n_{\text{H}} < 10 \text{ cm}^{-3}$ agrees well with the one derived by Jenkins (2009). Because of the fast electronic recombination of Cl^+ and its efficient reaction with H_2 , Cl^+ disappears efficiently even at very low density. The fact that we are able to reproduce the chlorine-observed depletion at very low density may indicate that the electronic recombination of other elements might be too low. Bryans et al. (2009) have tested the impact of new more accurate estimates of the electronic recombination of He^+ , C^+ , O^+ , Na^+ , and Mg^+ for a variety of physical conditions. According to their calculations, the largest difference between the new-rate coefficients and the ones typically listed in current astrochemical data bases was for Mg^+ electronic

recombination, which is 60 per cent smaller at 10 K in the new estimates. Such differences may not impact our calculations. However, it could be worth deriving parametrized rate coefficients from the original calculations to include them in astrochemical models. The authors also stated that there exist no reliable data for Si^+ , P^+ , S^+ , Cl^+ , and Fe^+ .

Possible explanations for discrepancies observed at low densities may also come from unaccounted processes in the current chemical model. A first possibility comes from the single grain-size approximation we make. For instance, an MRN-size distribution (from Mathis, Rumpl & Nordsieck 1977) extended down to $a_{\text{min}} \sim 10 \text{ \AA}$ decreases the collision time-scale between atoms and grains by a factor of ~ 6 (i.e. $t \sim 10^7 \text{ yr}$ at $n_{\text{H}} \sim 10 \text{ cm}^{-3}$). If we further take into account that a significant fraction of these small grains (which

dominate the surface area) would be negatively charged, Coulomb focusing reduces this time-scale to few 10^5 yr making possible the *in situ* depletion of some of the atomic cations (Weingartner & Draine 1999). The non-thermal desorption mechanism (though cosmic ray heating, for instance) would, however, reduce strongly the depletion effect of the small grains (Cuppen, Morata & Herbst 2006).

However, additional considerations such as the strength of the adsorption at the surface should also be explored. Even though enhanced collision rates could facilitate the depletion process, a fraction of these elements must remain bound to the surface at very low densities (this is especially true for elements such as Mg, Fe, P, and Si, for which significant depletion has been inferred at low densities). In the present study, we assumed physisorption for which typical binding energy varies between 10 and few 100 meV. Such low-binding energies lead relatively fast thermal desorption time-scale under diffuse cloud conditions. Indeed, we find that the combination of photoprocessing and thermal evaporation is efficient for clearing out the grain's surface from any adsorbed atoms and molecules on time-scales of few 10^4 yr at $n_H \sim 10$ cm $^{-3}$. The inclusion of chemisorption sites, characterized by increased binding energies (>0.1 eV), may be able to keep a significant fraction of these elements bound to the surface under diffuse cloud conditions and should thus be included in future studies. However, if chemisorption has been studied for hydrogen atoms, to the best of our knowledge, there exists little information on this process for other elements. In particular, the strength of chemisorption under high-irradiation conditions remains to be studied in detail.

On the other hand, if we assume that the diffuse ISM-observed depletion is due to depletion in dense regions that have been brought back into diffuse conditions, another possibility comes from the production of refractory material resulting from irradiation of the ice mantles during the transition between dense molecular clouds to diffuse clouds. Laboratory experiments on the irradiation of interstellar ice analogues have demonstrated an efficient formation of refractory compounds (e.g. Bernstein et al. 1995; Nuevo et al. 2011; Abou Mrad et al. 2015) and, in particular, material very similar to insoluble organic material found in meteorites and interplanetary dust particles (Nuevo et al. 2011). These residues should be relatively refractory to processes such as thermal evaporation and photodesorption (even though they may be altered by UV irradiation) under diffuse clouds conditions and could thus represent possible candidate for interstellar depletion carriers. Chemical networks that include such complexity remain to be developed.

ACKNOWLEDGEMENTS

VW's research was funded by an European Research Council Starting Grant (3DICE, grant agreement 336474). The authors acknowledge the CNRS program 'Physique et Chimie du Milieu Interstellaire' (PCMI) co-funded by the Centre National d'Etudes Spatiales (CNES). IAB acknowledges funding from the European Research Council for the FP7 ERC advanced grant project ECOGAL. This work used the DiRAC Complexity system, operated by the University of Leicester IT Services, which forms part of the STFC DiRAC HPC Facility (www.dirac.ac.uk). This equipment is funded

by BIS National E-Infrastructure capital grant ST/K000373/1 and STFC DiRAC Operations grant ST/K0003259/1. DiRAC is part of the National E-Infrastructure. MRõs research was supported by an appointment to the NASA Postdoctoral Program at the NASA Ames Research Center, administered by Universities Space Research Association under contract with NASA.

DATA AVAILABILITY

The physical and chemical simulations and the nautilus gas-grain model are available upon request.

REFERENCES

- Abou Mrad N., Vinogradoff V., Duverney F., Danger G., Theulé P., Borget F., Chiavassa T., 2015, *Bull. Soc. R. Sci. Liege*, 84, 21
- Asplund M., Grevesse N., Sauval A. J., Scott P., 2009, *ARA&A*, 47, 481
- Bel N., Lafon J. P. J., Viala Y. P., Loireleux E., 1989, *A&A*, 208, 331
- Bernstein M. P., Sandford S. A., Allamandola L. J., Chang S., Scharberg M. A., 1995, *ApJ*, 454, 327
- Bonnell I. A., Dobbs C. L., Smith R. J., 2013, *MNRAS*, 430, 1790
- Bryans P., Kreckel H., Roueff E., Wakelam V., Savin D. W., 2009, *ApJ*, 694, 286
- Cuppen H. M., Morata O., Herbst E., 2006, *MNRAS*, 367, 1757
- Draine B. T., 2009, in Henning T., Grün E., Steinacker J., eds, *ASP Conf. Ser. Vol. 414, Cosmic Dust – Near and Far*. Astron. Soc. Pac., San Francisco, p. 453
- Jenkins E. B., 2009, *ApJ*, 700, 1299
- Koyama H., Inutsuka S.-i., 2002, *ApJ*, 564, L97
- Larson R. B., 2005, *MNRAS*, 359, 211
- Mathis J. S., Rumpl W., Nordsieck K. H., 1977, *ApJ*, 217, 425
- McElroy D., Walsh C., Markwick A. J., Cordiner M. A., Smith K., Millar T. J., 2013, *A&A*, 550, A36
- Millar T. J., Bennett A., Rawlings J. M. C., Brown P. D., Charnley S. B., 1991, *A&AS*, 87, 585
- Neufeld D. A., Wolfire M. G., 2009, *ApJ*, 706, 1594
- Nuevo M., Milam S. N., Sandford S. A., De Gregorio B. T., Cody G. D., Kilcoyne A. L. D., 2011, *Adv. Space Res.*, 48, 1126
- Ruau M., Wakelam V., Hersant F., 2016, *MNRAS*, 459, 3756
- Ruau M., Wakelam V., Gratier P., Bonnell I. A., 2018, *A&A*, 611, A96
- Savage B. D., Sembach K. R., 1996, *ARA&A*, 34, 279
- Sofia U. J., Cardelli J. A., Savage B. D., 1994, *ApJ*, 430, 650
- Tielens A. G. G. M., 1998, *ApJ*, 499, 267
- Vázquez-Semadeni E., Gómez G. C., Jappsen A. K., Ballesteros-Paredes J., González R. F., Klessen R. S., 2007, *ApJ*, 657, 870
- Wakelam V. et al., 2012, *ApJS*, 199, 21
- Wakelam V., Ruau M., Gratier P., Bonnell I. A., 2019, *MNRAS*, 486, 4198
- Weingartner J. C., Draine B. T., 1999, *ApJ*, 517, 292
- Whittet D. C. B., 2010, *ApJ*, 710, 1009
- Ziurys L. M., Friberg P., Irvine W. M., 1989, *ApJ*, 343, 201

APPENDIX A: DUST AND GAS TEMPERATURES FOR TRAJECTORIES A AND B

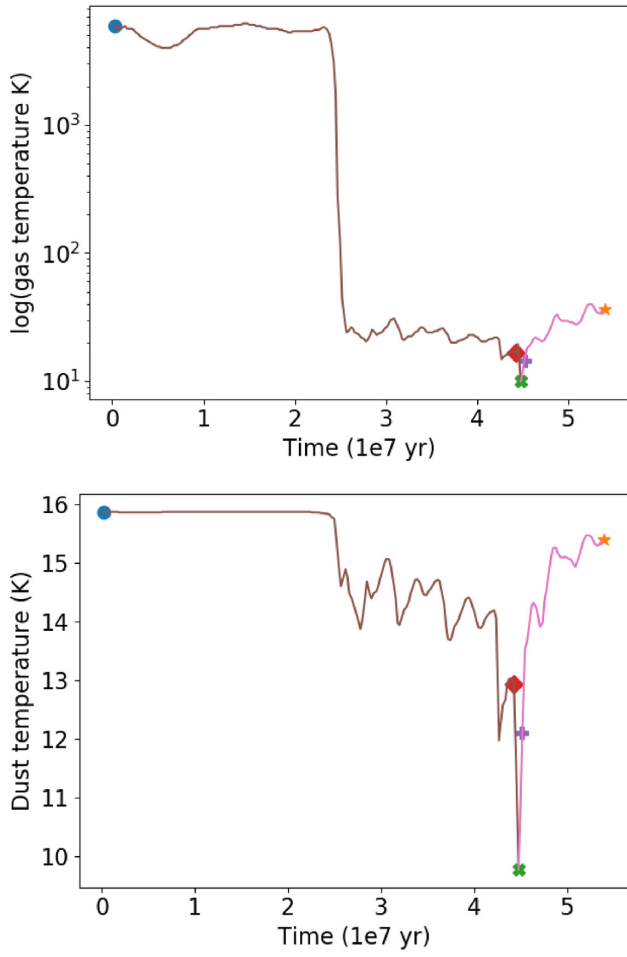


Figure A1. Gas and dust temperatures as a function of time for trajectory A.

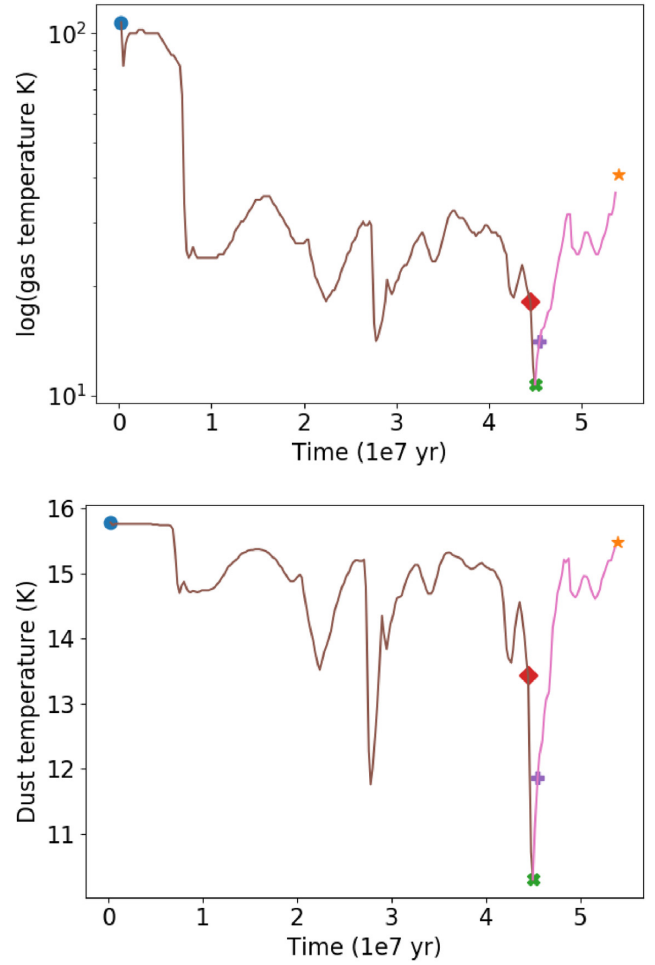


Figure A2. Gas and dust temperatures as a function of time for trajectory B.

This paper has been typeset from a $\text{\TeX}/\text{\LaTeX}$ file prepared by the author.